Research Article

Nano Research
2023, 16(7): 9022–9030

ISSN 1998-0124 CN 11-5974/O4
https://doi.org/10.1007/s12274-023-5668-0

In-situ study for the elastic structure evolutions of three-dimensional Ir-O framework during the oxygen evolution reaction in acid

Jun Qi[1], Xinyu Zhong[2,3], Huiyan Zeng[1], Chao Wang[1], Zhongfei Liu[1], Jiajun Chen[1], Long Gu[1], Enna Hong[1], Mengxian Li[1], Jiong Li[3,4] (✉), and Chunzhen Yang[1] (✉)

[1] *School of Materials, Shenzhen Campus of Sun Yat-Sen University, Shenzhen 518107, China*
[2] *Shanghai Institute of Applied Physics, Chinese Academy of Sciences, Shanghai 201204, China*
[3] *University of Chinese Academy of Sciences, Beijing 100049, China*
[4] *Shanghai Advanced Research Institute, Chinese Academy of Sciences, Shanghai 201210, China*

Received: 9 February 2023 / **Revised:** 10 March 2023 / **Accepted:** 12 March 2023

ABSTRACT

Understanding the dynamic structural and chemical evolutions at the catalyst–electrolyte interfaces is crucial for the development of active and stable electrocatalysts. In this work, β-Li_2IrO_3 is employed as a model catalyst for the oxygen evolution reaction (OER). Its elastic three-dimensional Ir-O framework enables us to investigate the Li^+ cation dissolution-induced structure evolutions and the formation mechanism of amorphous IrO_x species. Electrochemical measurements by rotating ring disk electrode (RRDE) reveal that up to 60% of the measured OER current can be ascribed to catalyst degradation. A series of *in-situ* X-ray diffraction spectroscopy (XRD), X-ray absorption spectroscopy (XAS), and Raman spectroscopy are conducted. Structure vibration is observed with oxidation states of Ir being reduced abnormally during OER at high potentials. It's hypothesized that the reversible proton intercalations are responsible for the Ir turn-over mechanism. Results of this work demonstrate a stable and elastic iridate structure and reveal the initial catalyst degradation behaviors during OER in acid media.

KEYWORDS

oxygen evolution reaction, structure evolution, amorphization, acid media, catalyst degradation

1 Introduction

Hydrogen production by electrocatalytic water splitting has been considered as one of the most promising technologies for green fuel production and better utilization of renewable energies. The oxygen evolution reaction (OER) at the anode is a key half-reaction for water electrolysis, which however limits the overall efficiency for the water electrolyzer, due to its sluggish reaction kinetics involving four proton-coupled electron transfers [1, 2]. Therefore, it is urgent to develop advanced catalysts with high activity and stability to promote the anodic OER performance. Unfortunately, only some Ir and/or Ru-based catalysts [3–6], such as perovskite $SrIrO_3$ [7] and pyrochlore iridates ($A_2Ir_2O_7$, A = Pb, Bi, and Y) [8, 9], can tolerate the extreme pH condition and highly oxidative environment during OER.

Most of the Ir-based catalysts still suffer surface corrosions to different levels along with composition and morphology changes during the OER in acidic media [10, 11]. This instability originates from cation dissolution, which is triggered by lowering of their coordination, resulting in rapid surface reconstruction and subsequent formation of amorphous or low crystalline (polycrystalline) species on the surface [12]. For example, Song et al. [13] show that leaching of alkaline-earth atoms is almost inevitable in acid electrolytes for the $AIrO_3$-type iridates (A = Sr and Ba). Suntivich's group [14] demonstrated that the crystalline-to-amorphous transformation of 3C-$SrIrO_3$ was triggered by lattice oxygen activation followed by Sr^{2+} dissolution from the structure. The deficient Sr^{2+} and O^{2-} sites further reorganized the surface structure. For developing stable OER catalysts, it is crucial to identify some stable crystalline structures that can tolerate sever cation dissolutions from the structure while maintaining its crystallinity during OER.

In addition, such surface reconstruction process during OER is so dynamic and uncontrollable. There is still limited knowledge about the initial reconstruction process [15–17]. Considering that the OER takes place on the outmost surface of catalyst particles, the newly formed species function as the real catalytic phases for water electrolysis. Zhang et al. [18] revealed that the amorphous RuO_x shells were formed during electrochemical oxidation on the surface of Ru-based alloys, which actually function as a passivation layer to inhibit Ru dissolution. Similarly, a stable self-reconstructed $IrO_x{\cdot}mH_2O$ was identified on the surface of Ir(V)-based perovskites. The hydrous iridate was proposed to form via a dissolution–reprecipitation mechanism [19]. Clearly, revealing the dissolution-induced structure evolutions and associated reaction intermediates formed on catalyst surface would bring more insights into the interfacial degradation mechanisms.

In this work, the β-Li_2IrO_3 oxide was employed as the model catalysts to study the Li^+-dissolution induced reconstruction and degradation during the OER in acid. There are two reasons for us

Address correspondence to Chunzhen Yang, yangchzh6@mail.sysu.edu.cn; Jiong Li, lijiong@sinap.ac.cn

to select the β-Li_2IrO_3 oxide as the model OER catalyst. Firstly, delithiation starts before OER and continuously during OER, which indeed mimics the alkaline cation dissolution process for many ABO_3 perovskite-type oxide catalysts. Importantly, the electrochemical potential for delithiation has been well determined in Li-ion batteries, which enables us to identify the startup potential of catalyst degradation and structure evolution. Secondly, the interconnected [IrO_6] octahedral units create a unique three-dimensional (3D) Ir-O framework which is chemically stable in strong acid. The sponge-like 3D structure consists of transportation channels for fast Li^+/H^+ exchange at the interface, thus provides a unique platform for us to investigate the structure stability and proton dynamics on catalyst surface. A series of *in-situ* characterization techniques were employed to investigate both surface and bulk changes during OER, including X-ray diffraction (XRD), Raman spectroscopy, and X-ray absorption fine structure (XAFS) spectroscopy. These *in-situ* spectroscopic techniques enable us to disclose the crucial structure and chemical information of electrocatalysts under acidic OER working conditions [20].

2 Experimental

2.1 Sample preparation

β-Li_2IrO_3 oxide was synthesized by a conventional solid-state reaction according to Refs. [21]. In a typical synthesis, commercial rutile-type IrO_2 (> 99.9%, Maclin) was mixed with equivalent Li_2CO_3 (≥ 99.0%, Sigma-Aldrich) homogeneously by throughly grinding in a mortar. The mixed precursor was then pressed into a pellet and kept in a corundum crucible for further calcination. The pellet was calcinated by heating at a ramping rate of 3 °C·min^{-1} to 1050 °C and holding for 12 h. The final β-Li_2IrO_3 product was prepared by repeated calcination, while the intermediate was fully ground for 20 min in a mortar.

2.2 Physical characterizations

XRD patterns were collected on an Empyrean diffractometer (Malvern-Panalytical Instrument) with Cu Kα radiations of λ (Kα1) = 1.540598 Å and λ (Kα2) = 1.544426 Å. Both *ex-situ* and *in-situ* XRD were conducted in this work. For *ex-situ* XRD measurements, the β-Li_2IrO_3 oxide was casted on carbon paper electrode with mass loading of 5 mg·cm^{-2}. Potentiostatic experiments were conducted at elevated potentials from open circuit voltage (OCV) to 1.65 V vs. reversible hydrogen electrode (RHE). Each potential of interest was held for 1 h in 0.5 M H_2SO_4 electrolyte. After rinsed by deionized (DI) water and dried in air, the reacted catalyst powder was scratched from the carbon paper electrode, and put in standard XRD sample holder for the measurement. *In-situ* XRD experiments were conducted on a home-designed electrochemical cell using Kapton® film as the transmitting X-ray window. The carbon paper electrode with β-Li_2IrO_3 catalyst was held at 1.6 V vs. RHE in 0.5 M H_2SO_4 electrolyte. After OER operation for each one minutes, the electrode was kept at open circuit potential, during which XRD profiles were collected.

In-situ XAFS measurements were conducted on a XAFS beamline (11B) in Shanghai Synchrotron Radiation Facility (SSRF) by a fluorescence mode. The Ir L_{III}-edge was measured with a beamline spot size of 250 μm, and photon flux reaching ~ 5×10^{11} photons·s^{-1}@10 keV. A Lytle detector was used to collect the fluorescence signals with a Zn plate as the filter. A home-designed electrochemical cell with a three-electrode configuration was constructed. The β-Li_2IrO_3 oxide was casted on carbon paper electrode with mass loading of 8 mg·cm^{-2}. Pt wire and Ag/AgCl (sat. KCl) electrode were adopted as the counter electrode and reference electrode, respectively. The catalyst electrode was holding at 1.6 V vs. RHE for water electrolysis. After OER operation for certain minutes, the electrode was kept at open circuit potential, during which XAFS spectra were collected. According to the beamline setup, it takes 8 min to record each XAFS spectrum. The corresponding potentiostatic curves were plotted in Fig. S1 in the Electronic Supplementary Material (ESM).

In-situ Raman spectroscopy measurements were conducted in a home-designed electrochemical cell using glassy carbon as working electrode and Pt wire as counter electrode, following the same electrochemical protocol as the *in-situ* XAFS measurement. Ag/AgCl (sat. KCl) electrode was used as the reference electrode. The β-Li_2IrO_3 catalyst paste was casted on the glassy carbon electrode. The working electrode was held at a potential of 1.6 V vs. RHE for 10 min in 0.5 M H_2SO_4 electrolyte. Raman spectra were collected during OCV after OER operation for every 1 min by using a 532 nm Laser source on the inVia Qontor spectrometer from RENISHAW. The laser intensity was maintained at 45 mW and the spectra were obtained by the accumulation of 3 spectral acquisitions with an exposure for 20 s.

High-resolution transmission electron microscopy (HR-TEM) was carried on a FEI Talos F200X microscope to check the surface crystal structure. Soft X-ray absorption spectra (sXAS) at the O K-edge were performed on the beamline BL11U station in Hefei NSRL. The X-ray photoelectron spectroscopy (XPS) was operated on the NEXSA instrument from Thermo Fisher.

2.3 Electrochemical measurements

All *operando* electrochemical measurements were carried out using a CHI760 potentiostat (Chenhua Instrument). The rotating ring disk electrode (RRDE) measurement was performed on a rotating system from Pine Instrument. The catalyst ink was dropcasted on the RRDE with a mass loading of 400 μg·cm^{-2}. The catalyst ink was prepared by mixing 10 mg of iridate powder with 5 wt.% acetylene carbon black and 30 μL Nafion ionomer (5% weight, Ion Power) in 1 mL of ethanol. A KCl-saturated Ag/AgCl electrode and a Pt wire were used as the reference electrode and counter electrode, respectively. The electrochemical setup of the RRDE measurement followed Ref. [22]. For the potentiostatic measurement, the disk electrode was held at 1.6 V vs. RHE at a rotating speed of 1600 rpm, during which the applied potential on the Pt ring electrode was set to 0.4 V vs. RHE for detecting O_2 generation at the disk electrode. Similarly, the disk electrode was also used for the cyclic voltammetry (CV) measurement at a scan rate of 10 mV·s^{-1} with rotation setting to 1600 rpm, and the Pt ring electrode was held continuously at 0.4 V vs. RHE. Ar gas was bubbled into the 0.5 M H_2SO_4 electrolyte before and during the RRDE measurements.

3 Results

3.1 Electrochemical behaviors

The β-Li_2IrO_3 oxide is a promising cathode material for Li-ion batteries [23], which demonstrated elastic structure evolutions during charge and discharge due to the reversible intercalation and deintercalation of Li^+ cations [21]. In order to confirm the degradation behavior as induced by cation (Li^+) dissolution during OER in acidic media, we conducted the RRDE measurement in 0.5 M H_2SO_4 solution as displayed in Fig. 1. The glassy carbon working electrode loading with β-Li_2IrO_3 oxide was used for the electrocatalytic water oxidation, whereas the platinum ring disk was kept at 0.4 V vs. RHE for the oxygen reduction reaction (ORR) (Figs. 1(b) and 1(c)). Commercial IrO_2 catalyst was also

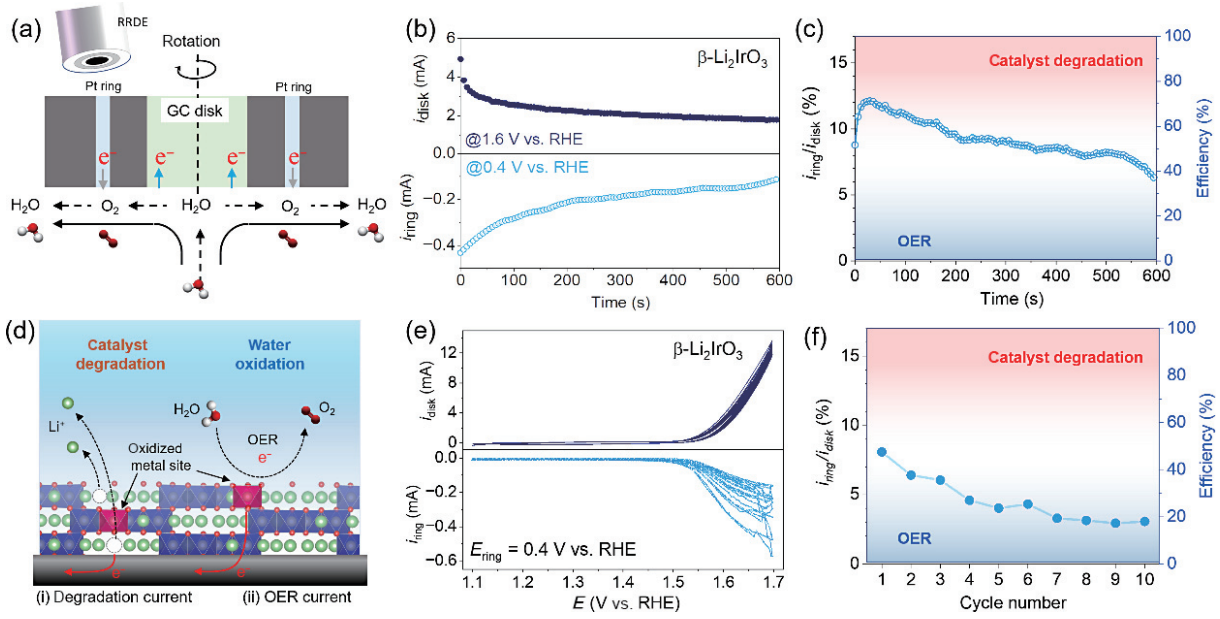

Figure 1 (a) The scheme of the RRDE measurements. (b) The potentiostatic measurement by holding the working electrode at 1.6 V vs. RHE for OER, while the Pt ring electrode holding at 0.4 V vs. RHE for the ORR. (c) The measured i_{ring}/i_{disk} efficiency. Right axis shows the current contributions which were estimated by taking the maximum 17% i_{ring}/i_{disk} efficiency as the system ability for O_2 detection. (d) The schematic illustration of the surface electrochemical processes involved during OER. (e) Cyclic voltammetry measurement and its corresponding ring current. (f) i_{ring}/i_{disk} efficiency at 1.6 V vs. RHE.

tested to estimate the system efficiency in the same experimental condition (Fig. S2 in the ESM). As for IrO_2, the efficiency for the platinum ring disc to capture the oxygen molecules electrochemically produced from the central working electrode was estimated to be 17%, which is in good agreement with Refs. [22, 24, 25]. Surprisingly, the β-Li_2IrO_3 catalyst exhibited very poor i_{ring}/i_{disk} efficiency, which achieved a maximum efficiency of 12%, then drastically decreased to ~ 6%. These values are much lower than that of commercial IrO_2 catalyst, suggesting the measured OER current indeed includes two contributions. If taking the 17% as the ideal system capability for O_2 detection, 60% of the measured OER current could come from the catalyst degradation, whereas only 40% was used for water oxidation. To confirm this conclusion, we further conducted cyclic voltammetry measurement (Figs. 1(e) and 1(f)). The measured i_{ring}/i_{disk} efficiency at 1.6 V vs. RHE was surprisingly low, which continuously decreased from 8% to about 3% along with cycling.

3.2 Bulk structure evolution

It is then essential to understand the current for catalyst degradation in the early stage which is ascribed to the delithiation process. A series of *ex-situ* XRD measurements were conducted to probe the possibly involved structure evolutions during OER. The β-Li_2IrO_3 electrode was treated at elevated potentials stepwise increased from OCV to 1.65 V vs. RHE in sulfuric acid by potentiostatic treatment for 1 h. As shown in Fig. 2(a), the structure starts to change since 0.92 V vs. RHE, which is equal to 3.95 V in the Li^+/Li scale. It is reasonable since at this potential, one equivalent of Li^+ would be delithiated from the bulk structure of the β-Li_2IrO_3 cathode in Li-ion battery. The structure transformation finished at 1.55 V vs. RHE. It is noted that the intensity of the diffraction peak centered at 20° as indexed to (004) crystal plane was drastically increased. But interestingly, the peak position was initially shifted to 19.2° and then to a higher degree of 19.5° beyond 1.4 V vs. RHE. The final structure is well maintained thereafter the OER operations over 1.55 V vs. RHE (Fig. 2(b)).

The β-Li_2IrO_3 possessed unique hyperhoneycomb structure with interconnected edge-sharing IrO_6 octahedra units forming a 3D Ir-O framework (Fig. S4 in the ESM). The 3D structure is indeed very stable, which can be thermally treated in 1 M H_2SO_4 acidic solution at 120 °C for complete Li^+/H^+ exchange [21]. Rietveld refinement was therefore conducted for these XRD profiles as shown in Fig. S5 in the ESM. The *ex-situ* XRD patterns measured at each interesting potential retain the hyperhoneycomb structure and can be indexed by the same Fddd space group. As Pearce et al. reported [23], β-Li_2IrO_3 could undergo symmetry structural evolution to the *C*2/*c* space group due to delithiation and formation of $Li_{0.5}IrO_3$ when increasing the electrochemical potential to 4.40 V vs. Li^+/Li. However, we did not observe such structure transformation during OER even at high potentials.

According to our Rietveld refinement, the estimated lattice distances of the (004), (220), and (111) facets were plotted versus electrode potentials (Fig. 2(c)). As shown in Fig. 2(d), the (004) crystal plane is perpendicular to the *C*-axis, while the (220) crystal plane is parallel to the *C*-axis. It is noted that the expansion of the [IrO_6]-[IrO_6] octahedral cluster between (004) crystal plane as well as the shrinkage of its perpendicular direction initiated at 0.92 V vs. RHE immediately. Further delithiation of β-Li_2IrO_3 above 1.40 V vs. RHE caused tight [IrO_6]-[IrO_6] connection. Overall, with increasing strain in the structure under the function of applied potentials, pronounced shrinkage of the channel space was observed. The β-Li_2IrO_3 demonstrated superior structure flexibility during the OER process.

When applying a high electrochemical potential directly on the catalyst, cation dissolution/catalyst oxidation would take place simultaneously along with the electrocatalytic OER process. *In-situ* XRD measurement was therefore conducted in a potentiostatic mode. As shown in Figs. 3(a)–3(c), we observed a fast structure change occurring within 1 min. Upon the electrooxidation, the β-Li_2IrO_3 might be dominated by the delithiation process in the early stage, which causes the structure self-regulation of the whole 3D framework to respond to oxidation. The β-Li_2IrO_3 (ICSD database code: 193972) and β-H_2IrO_3 [21] were employed for Rietveld fitting of the XRD patterns during structure transformation, so to identify the structure of those reacted oxides under working condition. Dramatic shifts of (111) and (004) peaks were observed on pristine β-Li_2IrO_3 and reacted oxides. During the OER operation, the intensity of (111) diffraction peak decreased rapidly while the (004) diffraction peak enhanced drastically.

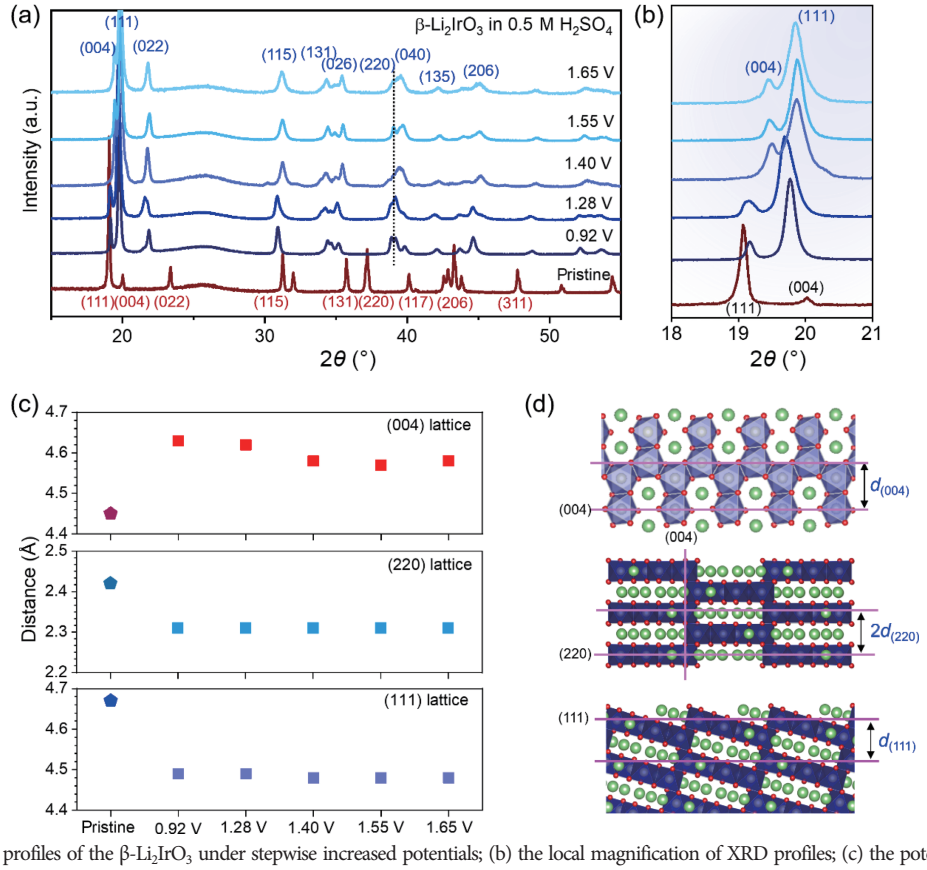

Figure 2 (a) The XRD profiles of the β-Li_2IrO_3 under stepwise increased potentials; (b) the local magnification of XRD profiles; (c) the potential dependent of local structure parameters of the β-Li_2IrO_3; and (d) different crystal facets of the 3D [IrO_6] framework.

To further gain the atomic arrangement and chemical states of Ir sites, we conducted the *in-situ* XAFS measurement at Ir L_{III}-edge by holding the electrode at 1.6 V vs. RHE. The corresponding X-ray absorption near-edge structure (XANES) spectra are plotted in Fig. 3(d). In general, the absorption peaks gradually shifted to higher energies along with OER, indicating the integral oxidation of Ir sites. We further analyzed the absorption peak positions versus the time in Fig. 3(e). According to the evolution of Ir chemical states, the structure evolution of β-Li_2IrO_3 during OER may involve two stages. In the initial 5 min, the absorption peaks shifted to higher energy positions, suggesting that the β-Li_2IrO_3 oxide undergoes a rapid oxidation probably accompanied by bulk delithiation from the structure. Afterwards, the absorption peak positions descended slightly in spite of the same operation condition, indicating the reduction of the Ir sites. After holding at 1.6 V vs. RHE for 20 min, the absorption peak stabilized at ~ 11,220 eV (Fig. S6 in the ESM). To analyze the changes in the local coordination environment, the *R* space was evaluated by the Fourier transform of the extended XAFS (EXAFS) spectra as plotted in Fig. 3(f). The β-Li_2IrO_3 catalyst at OCV demonstrated three major peaks located at 1.87, 2.87, and 3.43 Å, which are ascribed to the bond lengths of Ir–O, short Ir–Ir, and long Ir–Ir bonds, respectively. In our previous investigation, the pristine β-Li_2IrO_3 oxide possesses uniform Ir–O bond lengths throughout the whole bulk structure. Thus, it is therefore to hypothesize that the structure distortion starts when soaking the catalyst in sulfuric acid, which is in good agreement with the *ex-situ* XRD observations. The Ir–O bond lengths vary over time during OER operations, which firstly shrank, but eventually extended from 1.85 to 1.88 Å, revealing the dynamic oxidation/reduction behaviors of Ir sites during OER.

The turnover mechanism of Ir sites was firstly proposed by Minguzzi et al. [26]. By using *in-situ* X-ray absorption spectroscopy (XAS) measurement and proper XANES fittings, they identified that the high valence of Ir(V) can accumulate below the potential of OER onset, which further gets into fast Ir(V)/Ir(III) redox due to water oxidation. This is in line with the participation of the Ir sites in the heterogeneous Ir oxide catalyst in the catalytic cycle. For $E > 1.3$ V, Ir sites were presented in form of two distinct oxidation states, namely Ir(III) and Ir(V). Further increasing the potential to 1.5 and 1.6 V leads to the possibility of Ir(IV) in the catalytic cycle, which is proposed as a parenthesis of the Ir(V)/Ir(III) couple. The β-Li_2IrO_3 oxide demonstrated similar chemical reduction behavior due to chemical oxidation of water and simultaneous reduction of high-valence Ir species. According to Nong's research, the applied bias can accumulate the charge in the catalyst instead of directly acting on the reaction coordinate [1]. Considering that the XAFS measurement can be a bulk characterization technique, it is believed that the proton transfer promotes the bulk reduction of Ir site. We thus proposed the dynamic evolutions of Ir catalysts in Fig. 3(g).

3.3 Surface evolutions by Raman spectroscopy

The above *in-situ* XRD and XAFS measurements revealed the structure evolutions in the bulk catalyst. To gain more information of the reaction intermediates formed on catalyst surface, *in-situ* Raman spectroscopy was conducted at the same potentiostatic reaction condition. As shown in Fig. 4, the Raman spectrum of the β-Li_2IrO_3 oxide at OCV shows the typical vibration modes at 518 and 596 cm^{-1}. The lower band can be assigned to the out-of-phase vibrations of Li atoms along the *C*-axis [27]. According to the Raman analyses of the high-pressure experiment by Choi and his coworkers [28], the later band at 596 cm^{-1} is originated from the stretching vibrations of Ir-μ-oxo species, denoted as the A_g(O) vibration. In addition, three consecutive peaks featured at 724, 803, and 896 cm^{-1} are stemmed from the adventitious Nafion species, which are respectively assigned to the F–C–F symmetric stretching vibrations [29], the

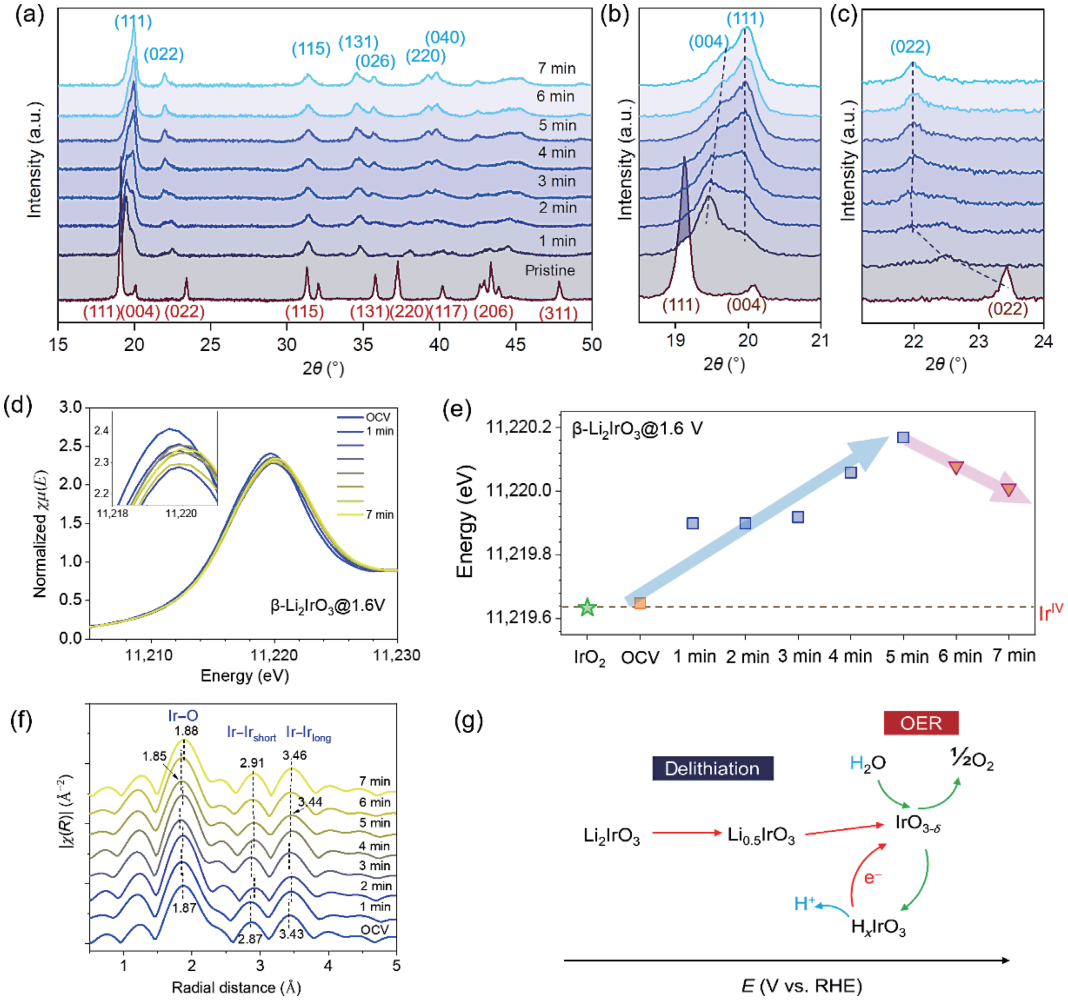

Figure 3 (a) *In-situ* XRD profiles of the β-Li_2IrO_3 operated at 1.6 V vs. RHE. (b) and (c) The local magnification of *in-situ* XRD profiles. (d) The evolution of the Ir L_{III}-edge XANES spectra during OER. (e) Absorption energies of the WL peak position. (f) The evolution of the Ir L_{III}-edge EXAFS spectra in *R* space. (g) Proposed turnover mechanism of reactive Ir sites which promote the chemical oxidation of water at high OER potentials.

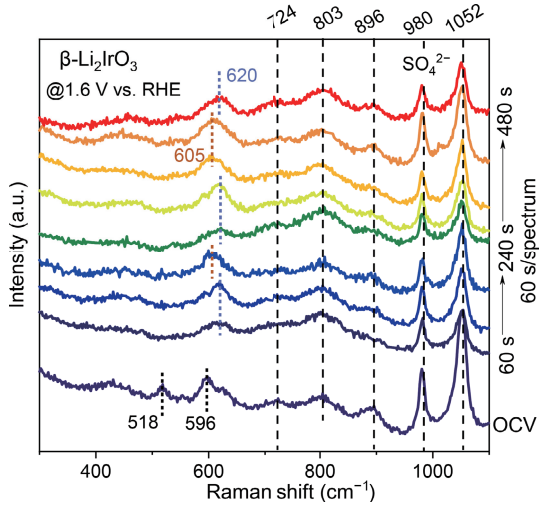

Figure 4 *In-situ* Raman spectra of the β-Li_2IrO_3 operated at 1.6 V vs. RHE.

C–S stretching vibration [30], and C–O–C ring stretching vibration [31] according to literatures. The bands with larger shifts centering at 980 and 1052 cm^{-1} are characteristics of the SO_4^{2-} anions in the electrolyte.

With no surprise, after 1 min of OER operation at 1.6 V vs. RHE, the band of the Li–O vibration completely disappeared, indicating a rapid delithiation process occurring on catalyst surface. The Ir-μ-oxo band shifted to higher positions of 620 cm^{-1} and vibrated between 605 and 620 cm^{-1} along with the OER test, which reflected the atomic vibrations on catalyst surface during OER. Since this A_g(O) band is ascribed to the Ir-μ-oxo species, the vibrations reflected the dynamic feature of the oxygen species on surface structure [28]. Pavlovic et al. [32] reported that a bule shift of the Ir-μ-oxo stretching vibration occurred from Ir(III)-Ir(IV) dimer to Ir(IV)-Ir(IV) dimer in the iridium oxo-hydroxo dimer complex. We claim that the shift of A_g(O) vibration to 605 cm^{-1} is probably owing to the electrooxidation of surface Ir–O species, while a blue shift to 620 cm^{-1} occurring at high potentials could be a strong indication for the turnover mechanism due to efficient reduction of oxidative Ir–O species at surface.

3.4 Surface degradation behaviors

The surface intermediates and chemical states were further analyzed by XPS and soft XAS. As shown in Fig. 5(a), there is no significant change on the Ir 4f spectra before and after the OER reaction. We fitted these XPS peaks by a doublet of the Ir $4f_{7/2}$ and Ir $4f_{5/2}$ peaks, together with a doublet of their satellite peaks and a second satellite of Ir $4f_{5/2}$ peak as shown in Fig. S7 in the ESM. The Ir $4f_{7/2}$ and Ir $4f_{5/2}$ peaks are located at 62.7 and 65.7 eV, respectively, which are identical to the values reported for iridium oxide nanoparticles by Minguzzi et al. [33]. Results suggested that the surface Ir sites maintained a relatively lower oxidation states (Ir(IV)) even after severe delithiation and oxidation. The O K-edge spectrum was also measured for the pristine and reacted β-Li_2IrO_3 (Fig. 5(b)), as well as rutile IrO_2 for a reference. The two

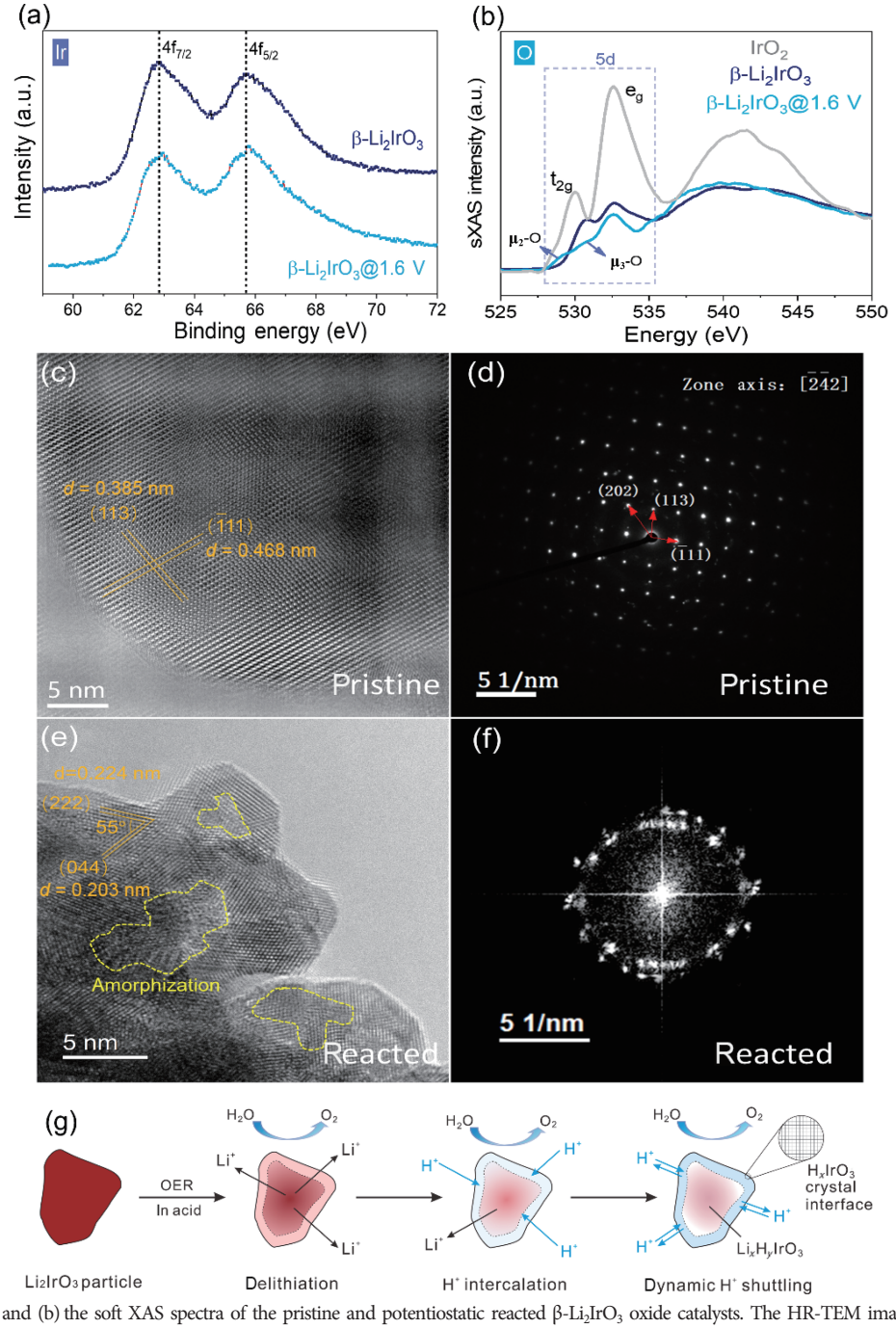

Figure 5 (a) The XPS and (b) the soft XAS spectra of the pristine and potentiostatic reacted β-Li_2IrO_3 oxide catalysts. The HR-TEM images of (c) the pristine β-Li_2IrO_3 and (e) potentiostatic reacted catalyst and corresponding SAED patterns are shown in (d) and (f), respectively. (g) Schematics of the electrochemical processes involved on the particles of β-Li_2IrO_3 during the potentiostatic OER measurement in acid.

pronounced resonances at 530.8 and 532.6 eV are ascribed to the t_{2g} and e_g states of Ir 5d bands hybridizing with the O 2p state, respectively. A crystal field of 1.8 eV is therefore estimated for pristine β-Li_2IrO_3 [34]. After the OER test, the reacted material shows weakening of the t_{2g} peak, whereas two distinctive μ_2-O and μ_3-O peaks appeared, which agrees with the observations on semicrystalline IrO_x by Mom and coworkers [35]. The formation of two O species indicates the inferior connectivity of distorted IrO_6 octahedron units on surface structure.

HR-TEM was employed to characterize the surface morphology and crystallinity of the degraded catalyst. As shown in Figs. 5(c)–5(f), the initial β-Li_2IrO_3 oxide particle shows a clean surface with well crystalized structure. The surface structure was also confirmed by the corresponding selected area electron diffraction (SAED) pattern along the [$\bar{2}\bar{4}2$] crystal zone axis. After the potentiostatic process at 1.6 V vs. RHE for 10 min, ordered atomic arrangement can be clearly observed on the exposed surface of reacted oxide particles, suggesting that the interface maintained a well crystallinity after structure transformation and cation exchanges. The corresponding SAED in Fig. 5(f) displays the annular diffraction spots which also proved the polycrystalline feature. Interestingly, distorted atomic arrangement can be observed at some regions at subsurface, as highlighted in Fig. 5(e). The amorphization seems to be initiated from the inner part of the catalyst. After a long-term OER operation, surface amorphization became serious as observed in most degraded OER catalysts with multiple small nanocrystals berried in the amorphous phases (Fig. S9 in the ESM). According to the CV curves of the β-Li_2IrO_3 as shown in Fig. S3 in the ESM, the OER activities of the catalyst gradually decrease along with cycling, whereas the electrochemical active surface area (ECSA) was observed to slightly decrease also, which is mainly due to surface amorphization and dissolution of

Ir metal sites. But basically, the existence of amorphization could not improve the intrinsic OER activity for the catalyst.

4 Discussion

So far, we have conducted a series of *in-situ* characterizations to probe the bulk and surface evolutions during OER on β-Li_2IrO_3 model catalyst. TEM revealed unique corrosion behaviors on catalyst surface. Three major findings are summarized and discussed here.

The 3D sponge-like Ir-O framework. The interconnected [IrO_6] octahedra units in β-Li_2IrO_3 form a very stable 3D [IrO_6] framework, which demonstrates stark elasticity during OER. According to our *in-situ* XRD measurements, delithiation from the bulk structure starts at low potentials (such as 0.92 V vs. RHE), suggesting that the cation leaching is unavoidable in sulfuric acid solution. During the OER operation, delithiation further induced slight structure distortion, but the strong edge- and face-sharing [IrO_6] connectivity appears to be maintained even after Li^+ leaching. The catalyst retained the *Fddd* space group within a broad potential range between 0.92–1.65 V vs. RHE. As demonstrated by Chang Woo et al. [36] on eleven different $A_xIr_yO_z$-type oxides (A = Ca, Sr, Ba, Y, Pr, and Nd), the intrinsic structure–property relationship in iridates was closely related to the [IrO_6] connection geometry and significantly affected the catalytic activity and stability during the OER. Interestingly, *in-situ* XRD measurements further revealed that it took about 5–7 min for the catalyst to completely transform to the final phase, whereas the surface delithiation completes within 1 min according to the *in-situ* Raman test. Clearly, the observed time discrepancy for delithiation is due to the diffusion limitation for Li^+ cations to transport from the bulk to the catalyst/electrolyte interfaces.

Measured OER current contains significant contribution from catalyst degradation. We previously [24] employed the electrochemical quartz microbalance microscopy (EQCM) to reveal the significant amount of cation leaching on Ni-based crystalline oxides, which leads to quick surface degradation and amorphization, resulting in amorphous Ni oxyhydroxide formation on oxide surface. Chang Woo et al. [13] studied the elemental dissolution of various ABO_3 perovskite oxides through atomic-scale direct probing by using high-resolution TEM. They identified that the surface structure could transform into metastable nanocrystallites or an amorphous state with substantial surface roughening induced by serious alkaline-earth elemental leaching. As a consequence, it has been generally agreed that the cation leaching would contribute to the OER current. In this work, the RRDE measurement further probed that there could be significant amount of current contribution (up to 60%) coming from the catalyst oxidation process, including the cation dissolution (as mimic the degradation process) and electrochemical oxidation of the bulk catalyst material. In an extreme condition, only less than 40% of the measured OER current was used to drive the "real" electrocatalytic reaction. Therefore, we would like to deliver a very important message to the community that the measured OER current may not be that accurate for evaluating the intrinsic catalytic activity of various OER catalysts, although it has been widely used so far.

Turnover mechanism associated with proton back-intercalation during OER. Interestingly, the *in-situ* XAFS measurement shows that the Ir sites were firstly oxidized followed by slightly reduction along with the OER operation. This phenomenon is similar to the turnover mechanism as discussed by Minguzzi et al. on the nanosized IrO_x catalysts [26, 37]. By means of *in-situ* XAS, they clearly revealed the co-existence of Ir(III) and Ir(V) at the electrode potentials where OER occurs. At 1.3 V, Ir reaches the highest oxidation state (V), whereas at higher potentials, i.e., for E > 1.5 and 1.6 V, Ir assumes two distinct oxidation states, namely (III) and (V). Yang et al. [38] employed a hydrated birnessite phase as the model catalyst, and discussed the electrochemical–chemical oxidation mechanism (EC mechanism) for OER. It is found that the reversible intercalations K^+ cations from the alkaline KOH solution into and out of the layer structure could promote the chemical oxidation of water and suppress the formation of Ir(V) oxide on catalyst surface. In our case, the Ir oxidation states were dominated by Ir(IV) as probed by our *in-situ* XANES and XPS analyses, whereas the bulk sites could be relatively higher. The electrochemical processes taking place on the particles of β-Li_2IrO_3 oxide were schematically illustrated in Fig. 5(g). When holding the catalyst at OER potentials for water oxidation, delithiation occurs immediately on catalyst surface, which is associated to the OER process. With more Li^+ leaching from the bulk structure, the average oxidation states of Ir gradually increase. We hypothesized that with the accumulation of high-valence Ir(V) sites on catalyst surface, the turnover mechanism and redox of Ir sites were triggered eventually via proton back-intercalation at the solid–liquid interfaces. In addition, we observed O–Ir–O vibrations shift up and down, corresponding to the expansion and shortage of the bond lengths, as characterized by *in-situ* Raman. The surface dynamics are probably involved with the rapid and reversible H^+ de-/intercalation. At extreme pH conditions, sufficient proton dynamics indeed stabilize the surface structure and suppress the formation of high-valence Ir species on catalyst surface, which may also contribute to maintain a well-crystallized interface of the hydrated catalyst during OER. Clearly, understanding the underlying mechanism could be significant for advancing stable OER catalysts in acid.

5 Conclusions

In summary, we have systematically investigated electrochemical properties and initial degradation behaviors of the β-Li_2IrO_3 oxide catalyst during OER in acid media. Its unique 3D interconnected Ir-O framework enabled us to investigate the cation leaching and initial structure evolutions at the early degradation stage during OER. Very importantly, we demonstrated that the degradation current could contribute for up to 60% of the measured OER current by using the RRDE measurement. Extra cautions should be taken when evaluating the intrinsic catalytic activity or activity benchmark for various catalysts by using the measured OER currents, either by cyclic voltammetry or potentiostatic measurement.

In addition, *in-situ* XAS measurement suggested a Ir turnover mechanism during OER, which is triggered by reversible intercalation and deintercalation of protons at the surface. It is also observed the O–Ir–O vibration mode shifting up and down by the *in-situ* Raman spectroscopy, which indicated the expansion and shortage of the Ir–O bond lengths as induced by proton dynamics at the catalyst surface. Overall, our results provide new insights into the understandings of the initial degradation processes and the vibrations of Ir chemical states and surface intermediates during OER.

Acknowledgements

We thank the Shanghai Synchrotron Radiation Facility (SSRF) BL-11B for the *in-situ* XAFS measurement and the National Synchrotron Radiation Laboratory (NSRL) beamline BL11U for the soft XAS measurement. C. Y. would like to acknowledge financial support from the National Natural Science Foundation of China (No. 21972172).

Electronic Supplementary Material: Supplementary material (further details of the Rietveld refinement, XPS fitting results, XAFS, and HR-TEM measurements by prolonging the operation on the β-Li_2IrO_3 oxide catalyst) is available in the online version of this article at https://doi.org/10.1007/s12274-023-5668-0.

References

[1] Nong, H. N.; Falling, L. J.; Bergmann, A.; Klingenhof, M.; Tran, H. P.; Spöri, C.; Mom, R.; Timoshenko, J.; Zichittella, G.; Knop-Gericke, A. et al. Key role of chemistry versus bias in electrocatalytic oxygen evolution. *Nature* **2020**, *587*, 408–413.

[2] Naito, T.; Shinagawa, T.; Nishimoto, T.; Takanabe, K. Recent advances in understanding oxygen evolution reaction mechanisms over iridium oxide. *Inorg. Chem. Front.* **2021**, *8*, 2900–2917.

[3] Chen, Y. B.; Li, H. Y.; Wang, J. X.; Du, Y. H.; Xi, S. B.; Sun, Y. M.; Sherburne, M.; Ager III, J. W.; Fisher, A. C.; Xu, Z. J. Exceptionally active iridium evolved from a pseudo-cubic perovskite for oxygen evolution in acid. *Nat. Commun.* **2019**, *10*, 572.

[4] Reier, T.; Pawolek, Z.; Cherevko, S.; Bruns, M.; Jones, T.; Teschner, D.; Selve, S.; Bergmann, A.; Nong, H. N.; Schlögl, R. et al. Molecular insight in structure and activity of highly efficient, low-Ir Ir-Ni oxide catalysts for electrochemical water splitting (OER). *J. Am. Chem. Soc.* **2015**, *137*, 13031–13040.

[5] She, L. N.; Zhao, G. Q.; Ma, T. Y.; Chen, J.; Sun, W. P.; Pan, H. G. On the durability of iridium-based electrocatalysts toward the oxygen evolution reaction under acid environment. *Adv. Funct. Mater.* **2022**, *32*, 2108465.

[6] Zu, L. H.; Qian, X. Y.; Zhao, S. L.; Liang, Q. H.; Chen, Y. E.; Liu, M.; Su, B. J.; Wu, K. H.; Qu, L. B.; Duan, L. L. et al. Self-assembly of Ir-based nanosheets with ordered interlayer space for enhanced electrocatalytic water oxidation. *J. Am. Chem. Soc.* **2022**, *144*, 2208–2217.

[7] Liang, X.; Shi, L.; Cao, R.; Wan, G.; Yan, W. S.; Chen, H.; Liu, Y. P.; Zou, X. X. Perovskite-type solid solution nano-electrocatalysts enable simultaneously enhanced activity and stability for oxygen evolution. *Adv. Mater.* **2020**, *32*, 2001430.

[8] Sun, W.; Liu, J. Y.; Gong, X. Q.; Zaman, W. Q.; Cao, L. M.; Yang, J. OER activity manipulated by IrO_6 coordination geometry: An insight from pyrochlore iridates. *Sci. Rep.* **2016**, *6*, 38429.

[9] Shih, P. C.; Kim, J.; Sun, C. J.; Yang, H. Single-phase pyrochlore $Y_2Ir_2O_7$ electrocatalyst on the activity of oxygen evolution reaction. *ACS Appl. Energy Mater.* **2018**, *1*, 3992–3998.

[10] Ruiz Esquius, J.; Algara-Siller, G.; Spanos, I.; Freakley, S. J.; Schlögl, R.; Hutchings, G. J. Preparation of solid solution and layered IrO_x-$Ni(OH)_2$ oxygen evolution catalysts: Toward optimizing iridium efficiency for OER. *ACS Catal.* **2020**, *10*, 14640–14648.

[11] Spöri, C.; Falling, L. J.; Kroschel, M.; Brand, C.; Bonakdarpour, A.; Kühl, S.; Berger, D.; Gliech, M.; Jones, T. E.; Wilkinson, D. P. et al. Molecular analysis of the unusual stability of an $IrNbO_x$ catalyst for the electrochemical water oxidation to molecular oxygen (OER). *ACS Appl. Mater. Interfaces* **2021**, *13*, 3748–3761.

[12] Simondson, D.; Chatti, M.; Bonke, S. A.; Tesch, M. F.; Golnak, R.; Xiao, J.; Hoogeveen, D. A.; Cherepanov, P. V.; Gardiner, J. L.; Tricoli, A. et al. Stable acidic water oxidation with a cobalt-iron-lead oxide catalyst operating via a cobalt-selective self-healing mechanism. *Angew. Chem., Int. Ed.* **2021**, *60*, 15821–15826.

[13] Song, C. W.; Suh, H.; Bak, J.; Bae, H. B.; Chung, S. Y. Dissolution-induced surface roughening and oxygen evolution electrocatalysis of alkaline-earth iridates in acid. *Chem* **2019**, *5*, 3243–3259.

[14] Wan, G.; Freeland, J. W.; Kloppenburg, J.; Petretto, G.; Nelson, J. N.; Kuo, D. Y.; Sun, C. J.; Wen, J. G.; Diulus, J. T.; Herman, G. S. et al. Amorphization mechanism of $SrIrO_3$ electrocatalyst: How oxygen redox initiates ionic diffusion and structural reorganization. *Sci. Adv.* **2021**, *7*, eabc7323.

[15] Liu, X.; Meng, J. S.; Zhu, J. X.; Huang, M.; Wen, B.; Guo, R. T.; Mai, L. Q. Comprehensive understandings into complete reconstruction of precatalysts: Synthesis, applications, and characterizations. *Adv. Mater.* **2021**, *33*, 2007344.

[16] Liu, X.; Guo, R. T.; Ni, K.; Xia, F. J.; Niu, C. J.; Wen, B.; Meng, J. S.; Wu, P. J.; Wu, J. S.; Wu, X. J. et al. Reconstruction-determined alkaline water electrolysis at industrial temperatures. *Adv. Mater.* **2020**, *32*, 2001136.

[17] Liu, J. Z.; Guo, L. *In situ* self-reconstruction inducing amorphous species: A key to electrocatalysis. *Matter* **2021**, *4*, 2850–2873.

[18] An, L.; Yang, F.; Fu, C. H.; Cai, X. Y.; Shen, S. Y.; Xia, G. F.; Li, J.; Du, Y. Z.; Luo, L. X.; Zhang, J. L. A functionally stable RuMn electrocatalyst for oxygen evolution reaction in acid. *Adv. Funct. Mater.* **2022**, *32*, 2200131.

[19] Zhang, R. H.; Dubouis, N.; Ben Osman, M.; Yin, W.; Sougrati, M. T.; Corte, D. A. D.; Giaume, D.; Grimaud, A. A dissolution/precipitation equilibrium on the surface of iridium-based perovskites controls their activity as oxygen evolution reaction catalysts in acidic media. *Angew. Chem., Int. Ed.* **2019**, *58*, 4571–4575.

[20] Long, C.; Han, J. Y.; Guo, J.; Yang, C. Y.; Liu, S. Q.; Tang, Z. Y. *Operando* toolbox for heterogeneous interface in electrocatalysis. *Chem Catal.* **2021**, *1*, 509–522.

[21] Pearce, P. E.; Yang, C. Z.; Iadecola, A.; Rodriguez-Carvajal, J.; Rousse, G.; Dedryvère, R.; Abakumov, A. M.; Giaume, D.; Deschamps, M.; Tarascon, J. M. et al. Revealing the reactivity of the iridium trioxide intermediate for the oxygen evolution reaction in acidic media. *Chem. Mater.* **2019**, *31*, 5845–5855.

[22] Filimonenkov, I. S.; Istomin, S. Y.; Antipov, E. V.; Tsirlina, G. A.; Savinova, E. R. Rotating ring-disk electrode as a quantitative tool for the investigation of the oxygen evolution reaction. *Electrochim. Acta* **2018**, *286*, 304–312.

[23] Pearce, P. E.; Perez, A. J.; Rousse, G.; Saubanère, M.; Batuk, D.; Foix, D.; McCalla, E.; Abakumov, A. M.; Van Tendeloo, G.; Doublet, M. L. et al. Evidence for anionic redox activity in a tridimensional-ordered Li-rich positive electrode β-Li_2IrO_3. *Nat. Mater.* **2017**, *16*, 580–586.

[24] Yang, C. Z.; Batuk, M.; Jacquet, Q.; Rousse, G.; Yin, W.; Zhang, L. T.; Hadermann, J.; Abakumov, A. M.; Cibin, G.; Chadwick, A. et al. Revealing pH-dependent activities and surface instabilities for Ni-based electrocatalysts during the oxygen evolution reaction. *ACS Energy Lett.* **2018**, *3*, 2884–2890.

[25] Köhler, L.; Abrishami, M. E.; Roddatis, V.; Geppert, J.; Risch, M. Mechanistic parameters of electrocatalytic water oxidation on $LiMn_2O_4$ in comparison to natural photosynthesis. *ChemSusChem* **2017**, *10*, 4479–4490.

[26] Minguzzi, A.; Lugaresi, O.; Achilli, E.; Locatelli, C.; Vertova, A.; Ghigna, P.; Rondinini, S. Observing the oxidation state turnover in heterogeneous iridium-based water oxidation catalysts. *Chem. Sci.* **2014**, *5*, 3591–3597.

[27] Glamazda, A.; Lemmens, P.; Do, S. H.; Choi, Y. S.; Choi, K. Y. Raman spectroscopic signature of fractionalized excitations in the harmonic-honeycomb iridates β- and γ-Li_2IrO_3. *Nat. Commun.* **2016**, *7*, 12286.

[28] Choi, S.; Kim, H. S.; Kim, H. H.; Krajewska, A.; Kim, G.; Minola, M.; Takayama, T.; Takagi, H.; Haule, K.; Vanderbilt, D. et al. Lattice dynamics and structural transition of the hyperhoneycomb iridate β-Li_2IrO_3 investigated by high-pressure Raman scattering. *Phys. Rev. B* **2020**, *101*, 054102.

[29] Bribes, J. L.; El Boukari, M.; Maillols, J. Application of Raman spectroscopy to industrial membranes. Part 2—Perfluorosulphonic membrane. *J. Raman Spectrosc.* **1991**, *22*, 275–279.

[30] El Boukari, M.; Bribes, J. L.; Maillols, J. Application of Raman spectroscopy to industrial membranes. Part 1—polyacrylic membranes. *J. Raman Spectrosc.* **1990**, *21*, 755–759.

[31] Ethève, J.; Huguet, P.; Innocent, C.; Bribes, J. L.; Pourcelly, G. Electrochemical and Raman spectroscopy study of a nafion perfluorosulfonic membrane in organic solvent-water mixtures. *J. Phys. Chem. B* **2001**, *105*, 4151–4154.

[32] Pavlovic, Z.; Ranjan, C.; Gao, Q.; van Gastel, M.; Schlögl, R. Probing the structure of a water-oxidizing anodic iridium oxide catalyst using Raman spectroscopy. *ACS Catal.* **2016**, *6*, 8098–8105.

[33] Minguzzi, A.; Locatelli, C.; Lugaresi, O.; Achilli, E.; Cappelletti, G.;

Scavini, M.; Coduri, M.; Masala, P.; Sacchi, B.; Vertova, A. et al. Easy accommodation of different oxidation states in iridium oxide nanoparticles with different hydration degree as water oxidation electrocatalysts. *ACS Catal.* **2015**, *5*, 5104–5115.

[34] Tsai, H. M.; Babu, P. D.; Pao, C. W.; Chiou, J. W.; Jan, J. C.; Kumar, K. P. K.; Chien, F. Z.; Pong, W. F.; Tsai, M. H.; Chen, C. H. et al. Comparison of electronic structures of RuO_2 and IrO_2 nanorods investigated by X-ray absorption and scanning photoelectron microscopy. *Appl. Phys. Lett.* **2007**, *90*, 042108.

[35] Mom, R. V.; Falling, L. J.; Kasian, O.; Algara-Siller, G.; Teschner, D.; Crabtree, R. H.; Knop-Gericke, A.; Mayrhofer, K. J. J.; Velasco-Vélez, J. J.; Jones, T. E. *Operando* structure–activity–stability relationship of iridium oxides during the oxygen evolution reaction. *ACS Catal.* **2022**, *12*, 5174–5184.

[36] Song, C. W.; Lim, J.; Bae, H. B.; Chung, S. Y. Discovery of crystal structure–stability correlation in iridates for oxygen evolution electrocatalysis in acid. *Energy Environ. Sci.* **2020**, *13*, 4178–4188.

[37] Bozal-Ginesta, C.; Rao, R. R.; Mesa, C. A.; Liu, X. Y.; Hillman, S. A. J.; Stephens, I. E. L.; Durrant, J. R. Redox-state kinetics in water-oxidation IrO_x electrocatalysts measured by *Operando* spectroelectrochemistry. *ACS Catal.* **2021**, *11*, 15013–15025.

[38] Yang, C. Z.; Rousse, G.; Louise Svane, K.; Pearce, P. E.; Abakumov, A. M.; Deschamps, M.; Cibin, G.; Chadwick, A. V.; Dalla Corte, D. A.; Anton Hansen, H. et al. Cation insertion to break the activity/stability relationship for highly active oxygen evolution reaction catalyst. *Nat. Commun.* **2020**, *11*, 1378.